CTFFIND5 provides improved insight into quality, tilt and thickness of TEM samples

Johannes Elferich [a, b,*], Lingli Kong [a], Ximena Zottig [a,b], Nikolaus Grigorieff [a,b,*]

[a] RNA Therapeutics Institute, University of Massachusetts Chan Medical School RNA Therapeutics Institute

[b] Howard Hughes Medical Institute

[*] Correspondence: johannes.elferich@umassmed.edu, niko@grigorieff.org

Abstract

Images taken by transmission electron microscopes are usually affected by lens aberrations and image defocus, among other factors. These distortions can be modeled in reciprocal space using the contrast transfer function (CTF). Accurate estimation and correction of the CTF is essential for restoring the high-resolution signal in an image and has been one of the key aspects of the "resolution revolution" in cryogenic electron microscopy (cryoEM). Previously, we described the implementation of algorithms for this task in the *cis*TEM software package (Grant *et al.*, 2018). Here we show that taking sample characteristics, such as thickness and tilt, into account can improve CTF estimation. This is particularly important when imaging cellular samples, where measurement of sample thickness and geometry derived from accurate modeling of the Thon ring pattern helps judging the quality of the sample. This improved CTF estimation has been implemented in CTFFIND5, a new version of the *cis*TEM program CTFFIND. We evaluated the accuracy of these estimates using images of tilted aquaporin crystals and eukaryotic cells thinned by focused ion beam milling. We estimate that with micrographs of sufficient quality CTFFIND5 can measure sample tilt with an accuracy of 3° and sample thickness with an accuracy of 5 nm.

Introduction

Transmission electron microscopy of biological specimens at cryogenic temperatures (cryoEM) has become a widely used method to image biomolecules at high resolution, both in solution and within the cell. To retrieve the high-resolution signal, the cryoEM images have to be corrected for the contrast-transfer function (CTF) of the microscope. Common parameters used to describe the CTF include an astigmatic defocus, the spherical aberration of the objective lens, and if appropriate, a phase shift introduced by a phase plate. These parameters are commonly estimated by fitting the Thon ring pattern (Thon, 1971) in the power spectrum of micrographs to a modeled power spectrum. The program CTFFIND4 (Rohou & Grigorieff, 2015) has been developed for this task and the model and conventions to describe the CTF are widely adopted in the field.

A limitation of CTFFIND4 is that it considers the whole imaged sample to be at the same objective defocus, which is a reasonable assumption for flat and thin samples, as is common in single-particle cryoEM. However, the increased thickness of cryoEM samples of cells may introduce additional modulations in the Thon ring pattern (Tichelaar *et al.*, 2020) that can lead to errors in the CTF modeling when not accounted for. Furthermore, samples of cells are often tilted with respect to the optical axis of the microscope, either unintentionally due to thinning methods such as cryogenic focused ion beam (FIB) milling, or intentionally during electron cryo-tomography imaging. In both cases the effects are strongest at high-resolution, where the Thon rings are more tightly spaced.

Here we describe new features of CTFFIND5 that can fit the modulations of the Thon ring patterns and determine sample thickness and tilt using an extended CTF model with additional parameters. This not only increases the fidelity of the fit, as Thon rings at higher resolution can now be fitted reliably, but also gives valuable insight into the geometry of the sample that can aid the experimentalist.

Methods

Tilt estimation algorithm

Tilt estimation in CTFFIND5 follows a strategy that is similar to the implementation in CTFTILT (Mindell & Grigorieff, 2003). The tilt axis direction ϕ and tilt angle θ are determined by fitting Thon ring patterns locally, calculated from 128 x 128 pixel tiles that form a regular grid covering the micrograph (Fig. 1a). In this model, ϕ has a positive value ranging from 0° to 360° to describe the angle to the X-axis of the micrograph. It is assumed that the defocus variation across the sample can be described by a tilted plane. Fits are evaluated using correlation coefficients between modeled CTFs and Thon ring patterns. Initially, the micrograph pixel size is adjusted (binned) by Fourier cropping to match the resolution limit of the fit set by the user and the micrograph is cropped to be square in order to speed up computation. A power spectrum is calculated from this binned and cropped image, a smooth background is calculated using a box convolution (Mindell & Grigorieff, 2003) and subtracted, the power spectrum is further binned to the tile size (128 x 128 pixels), and the fit of the tilted Thon ring patterns across the micrograph is initialized by fitting this highly binned power spectrum with a non-astigmatic CTF. This fit is then refined using a two-dimensional CTF with astigmatism. Rough values for the tilt axis and angle are then determined in a systematic search in 10° and 5°, respectively, using the locally fitted Thon ring patterns to score each pair of tilt axis and angle, followed by local refinement of tilt axis, angle and average defocus.

Finally, an average tilt-corrected power spectrum is calculated for diagnostic purposes and to allow the determination of a fit resolution. The tilt correction is designed to remove most of the Thon ring blurring due to the defocus variation across the image. To minimize ring blurring, the power spectrum from each tile is adjusted according to its local average defocus, $\Delta f_{average}$, by magnifying it by a factor m with

$$m = \sqrt{\Delta f_{local} / \Delta f_{average}} \qquad (1)$$

Since Δf_{local} will assume values across the image that are both smaller and larger than $\Delta f_{average}$, m will assume values smaller and larger than 1. The magnification / demagnification of the power spectrum compensates for the contraction / expansion of the Thon rings due to the local defocus change and produces approximately constant Thon ring patterns that can be averaged without losing the pattern (Fig. 1b). The compensation will have a small error if the spherical aberration is not zero. However, this error is sufficiently small to not visibly affect the Thon rings in the average.

Verification of tilt estimation using tilted aquaporin crystals

To test the robustness and accuracy of the new fitting algorithm, the defocus and sample tilts of aquaporin 2D crystals (Murata *et al.*, 2000) were estimated using a search range from 5000 Å to 50000 Å and a 100 Å step, low and high resolution limits of 30 Å to 5 Å, respectively, and a box size for the final power spectrum of 512 pixels. The estimated tilt angle θ and axis direction ϕ were compared with the values obtained by 2D crystallographic processing (Mindell & Grigorieff, 2003).

Verification of tilt estimation using tilt series

Lamellae prepared by FIB milling usually exhibit a pre-tilt with respect to the grid surface due to the stage tilt in the FIB instrument. In the microscope, the direction of this pre-tilt will generally not line up with the goniometer tilt axis. For the alignment of a tomogram recorded from such a lamella, the relative orientation of these two axes will have to be determined, together with the precise amount of pre-tilt. We wrote a new *cis*TEM (Grant *et al.*, 2018) program, called fit_tilt_model, to read the tilt angles and axes determined for each image in a tomographic tilt series and fit them to a model incorporating a pre-tilt and a single tomographic tilt axis. Using a rotation matrix R_0 to represent the pre-tilt and rotation matrices R_{tom}^{i} to represent the tomographic tilt angles and axis read from the microscope, the overall sample orientations are given by

$$R^i = R_0 \times R^i_{tom} \qquad (2)$$

R_0 and R^i_{tom} are calculated from the tilt angles θ and axes ϕ as

$$R = \begin{bmatrix} \cos(\phi)^2 + \sin(\phi)^2\cos(\theta) & \cos(\phi)\sin(\phi)\,(\cos(\theta) - 1) & -\sin(\phi)\sin(\theta) \\ \cos(\phi)\sin(\phi)\,(\cos(\theta) - 1) & \cos(\phi)^2\cos(\theta) + \sin(\phi)^2 & -\cos(\phi)\sin(\theta) \\ \sin(\phi)\sin(\theta) & \cos(\phi)\sin(\theta) & \cos(\theta) \end{bmatrix} \qquad (3)$$

In CTFFIND5, both tilt axis and angle are defined in the clockwise direction, with the angle of the axis measured from the x-axis. This may be different from the definition used by the microscope. To ensure consistency with the widely accepted angular convention in the cryoEM field, all the θ and ϕ used in this manuscript refer to an anti-clockwise direction, with ϕ measured from the x-axis.

Using the tilt information obtained with CTFFIND5, we now have a set of rotation matrices R^i, and together with the rotation matrices read from the microscope, R^i_{tom}, we can calculate a set of pre-tilt estimates R^i_0 from equation (2). To determine the best overall pre-tilt R_0, we determine the plane-normal vectors $V^i_{norm} = [x, y, z]$ of the sample by applying R^i_0 to the vector [0,0,1] (z-coordinate along the beam direction), followed by calculating their mean $V^{mean}_{norm} = [x_o,\ y_0,\ z_0]$ as the normal vector of the best overall pre-tilt estimate. By calculating the root mean squared deviation of the normal vectors V^i_{norm}, outliers can be identified and excluded to further refine V^{mean}_{norm}. The pre-tilt can then be determined as:

$$\theta_0 = \begin{cases} \cos^{-1}(z_0) & x_0 \geq 0 \\ -\cos^{-1}(z_0) & x_0 < 0 \end{cases}$$
$$\phi_0 = \begin{cases} \tan^{-1}(\frac{x_0}{y_0}) & y_0 \neq 0, \phi_0 \in [0,180] \\ 90° & y_0 = 0 \end{cases} \qquad (4)$$

To generate more reliable defocus and tilt estimates, the defocus search range and resolution fitting range can be adjusted according to the experimental tilt range and image quality. For our cryoEM samples, the low and high resolution limits were set to 50 Å to 10 Å, respectively, and the defocus search interval was set to be between $\pm$ 10000 and $\pm$20000 Å from the nominal defocus set during data collection.

Sample thickness estimation

In CTFFIND5 we implemented a new CTF_t model function, based on the CTF function implemented in CTFFIND4 (Rohou & Grigorieff, 2015) and extended by the formula described by (McMullan *et al.*, 2015):

$$CTF_t(\lambda, \mathrm{g}, \Delta f, C_s, \Delta\varphi, \omega_2, t) = \frac{1}{2}\Big(1 - \mathrm{sinc}\big(\xi(\lambda, \mathrm{g}, t)\big)\cos\big(2\chi(\lambda, |\mathrm{g}|, \Delta f, C_s, \Delta\varphi, \omega_2)\big)\Big) \qquad (5)$$

where χ denotes the phase-shift as a function of the electron wavelength λ, the spatial frequency vector |g|, the objective defocus Δf, the spherical aberration C_s, the additional phase shift $\Delta\varphi$, and the fraction of amplitude contrast ω_2. The modulation of the CTF due to sample thickness t is described by the function ξ:

$$\xi(\lambda, \mathrm{g}, t) = \pi\lambda \mathrm{g}^2 t \qquad (6)$$

If a user requests sample thickness estimation, the program will first fit the CTF model function as implemented in CTFFIND4 and the "goodness of fit" resolution will be used as an estimate of the frequency g of the first node of the CTF_t function, with t given by:

$$t = {}^{1}/_{\lambda \mathrm{g}^2} \qquad (7)$$

If the option "Brute-force 1D fit" is selected, CTFFIND5 will further refine t and Δf by calculating the normalized cross-correlation between the radial average of the power spectrum (corrected for astigmatism, as described in) and CTF_t, searching systematically for the best combination of t in the range of 50-400 nm in 10 nm steps, and Δf in the range of $\pm$200 nm from the previously fitted value, also in 10 nm steps.

Finally, if the option "2D-refinement" is selected, CTFFIND5 will optimize t, Δf_1, Δf_2, and ω using the same conjugate gradient algorithm used in CTFFIND4 and the normalized cross correlation between CTF_t and the 2D power spectrum as a scoring function.

After the optimal values for t and Δf have been obtained the "goodness of fit" crosscorrelation is recalculated using CTF_t, with a frequency window that is 1.5 time larger than in CTFFIND4 to avoid the drop-off in the node regions of CTF_t.

Verification of sample thickness estimation using Lambert-Beer's law

We used 655 micrographs collected from one lamella of ER-HoxB8 cells (dataset Lamella$_{EUC}$1 from (Elferich *et al.*, 2022)). For each micrograph we calculated $ln\left(\frac{I}{I_0}\right)$, where I was the sum of all pixels in the illuminated area of the movie and I_0 was the average of this sum for 45 micrographs collected over vacuum with the same energy filter settings. This value is expected to have a linear relationship with the thickness of the sample consistent with Lambert-Beer's law (Yan et al. 2015; Rice et al. 2018):

$$ln\left(\frac{I}{I_0}\right) = \frac{1}{\kappa}t \qquad (8)$$

where κ is the apparent mean free path for inelastic scattering.

We then used CTFFIND5 to estimate the thickness t of each micrograph using the "Brute-force 1D fit" and "2D-refinement" setting, low and high resolution limits set to 30 Å and 5 Å,

176 defocus search range set between 500 nm and 5000 nm, and low and high resolution limits
177 for thickness estimation set to 10 Å and 3 Å. We used a "RANSAC" algorithm as
178 implemented by the scikit-learn Python package (Pedregosa *et al.*, 2011) to fit a linear
179 model to the relationship of $ln\left(\frac{I}{I_0}\right)$ and t, while rejecting outliers. We then manually
180 inspected every outlier of the model fit and categorized the reason for the discrepancy into
181 "Occluded beam" (either from contamination or the edges of the lamella), "Low image
182 signal" (in most cases exposures containing no cellular features), "Carbon/Platinum", and
183 "Lipid droplet" (see Fig. 4).

184 **Verification of sample thickness estimation using tomography**

185 Lamellae prepared from ER-HoxB8 cells were imaged using a Titan Krios 300 keV TEM
186 controlled by SerialEM (Mastronarde, 2005). For each dataset an initial exposure was taken
187 with a magnification of 64,000, resulting in a pixel size of 1.6 Å and an exposure of 30 e^-/Å.
188 This was followed by the acquisition of a tilt series at a magnification of 48,000, resulting in
189 a pixel size of 2.087 Å. A total of 35 tilt images at a tilt interval of 3° were collected from -
190 51° to 51°, relative to the milling angle, using a grouped dose-symmetric scheme (Hagen *et*
191 *al.*, 2017). The exposure per tilt was 3 e^-/Å, resulting in a total exposure of 105 e^-/Å .

192 For tomographic reconstruction, tilt movie frame motion correction was performed using
193 SerialEM (Mastronarde, 2005), and tilt series were aligned using the IMOD software
194 package (version 4.11, Mastronarde & Held, 2017). For coarse alignment, a high-frequency
195 cutoff radius of 0.15 was used. A fiducial model was generated using patch tracking with
196 patches of 450 x 450 pixels and a fractional overlap of patches of 0.33 x 0.33. High-tilt
197 frames were omitted while generating the fiducial model. Robust fitting with a tuning
198 factor of 1 was used for fine alignment. After computing the alignment, the fiducial model
199 was edited by removing unreliable patches, and then alignments were re-computed. The
200 edited models with the lowest residual mean errors and standard deviations were used for
201 fine alignment. Tomogram positioning was used to correct the tilt angle offset. Fully aligned
202 stacks were generated with a binning factor of 4, resulting in a tomogram pixel size of 8.3 Å.
203 Tomograms were reconstructed using the SIRT-like filtering option in IMOD (Mastronarde

204 & Held, 2017; Mastronarde, 1997) and manually inspected. The tomograms were back-
205 projected along the y-axis using a homemade script, generating a small set of XZ
206 projections. Thickness measurements on the projected central slides were performed using
207 the display program included with the *cis*TEM software package (Grant *et al.*, 2018).

208 **CTF correction of medium magnification lamella images**

209 The CTF of the representative medium magnification image with a pixel size of 40 Å was
210 estimated using CTFFIND5 with the following parameters: defocus range: 1,000,000 to
211 4,000,000 Å; search step 50,000 Å; low and high resolution limits: 400 Å and 80 Å. We then
212 used the program apply_ctf, included with *cis*TEM, to flip the phases according to the
213 estimated CTF. We furthermore implemented the Wiener like filter described in (Tegunov
214 & Cramer, 2019) in apply_ctf to produce the image shown in Fig. 6d.

215 **Benchmarking CTFFIND5 runtimes**

216 CTFFIND5 runtimes were measured using 3 representative micrographs (Table 2). As a
217 baseline measurement, CTFFIND5 was run without estimation of tilt and sample thickness
218 enabled. Then runtime was measured enabling either one of these option or both. Every
219 test was repeated four times and the average and standard deviation of the last three runs
220 are reported, to minimize the contribution of hard-drive speed. The tests were performed
221 on a single core of an Intel Core i9-12900KF CPU.

222 ## Results

223 **Tilt estimation**

224 We tested the defocus correction for the Thon rings on a representative micrograph taken
225 from a cryo-FIB milled lamella. As expected, the correction results in the observation of
226 Thon rings at higher spatial resolution (Fig. 1c). In this example, correcting for the
227 estimated moderate tilt of 12.3° improved the highest resolution at which a reasonable fit
228 could be obtained from 5.9 Å to 4.6 Å. The power spectrum also appears less noisy, which
229 can be attributed to some low-pass filtering that occurs with the interpolation of the Thon
230 ring patterns of individual tiles to perform the defocus correction.

231 To test the performance of the new CTFFIND5 sample tilt estimation, we used a dataset of
232 images of tilted aquaporin crystals that were also used to benchmark the original CTFTILT
233 implementation (Mindell & Grigorieff, 2003; Murata *et al.*, 2000). Table 1 compares the tilt
234 information of the samples obtained from crystallographic analysis and the estimates
235 obtained using CTFFIND5. Overall, the results of CTFFIND5 agree well with the aquaporin
236 crystals information. The average discrepancy was 1.9° for the tilt axis direction and 1.5°
237 for the tilt angle.

238 To test whether CTFFIND5 would be able to correctly assign tilt axis and angle for tilt
239 series data, we analyzed two tilt series from different grids of lamellae prepared by cryo-
240 FIB milling from mouse neutrophil-like cells (Elferich *et al.*, 2022). We then plotted the
241 estimated values for tilt axis and angle as a function of nominal stage tilt (Fig. 2). The
242 estimated tilt angle shows a roughly linear relationship with the nominal stage tilt, but
243 since CTFFIND5 reports only positive tilt angles the overall plot has a chevron-shape. The
244 estimated tilt axis angle is approximately constant at high tilts but changes by about 180° at
245 0° estimated tilt, again due to the convention enforced by CTFFIND5. Notably, in both
246 examples there is an offset of about 20° between nominal and estimated tilts, which is due
247 to the pre-tilt of the specimen caused by FIB-milling at a shallow angle. To quantify and
248 delineate both the tilt axis direction of the microscope and the pre-tilt of the specimen we
249 fit all values to a model as described in Methods (Fig. 2). The fitting resulted in an
250 estimated tilt axis angle of 178.2° and 179.8°, respectively, which is consistent with the
251 SerialEM calibration of 178.4° and 176.3° for the stage tilt axis. The estimated pre-tilt
252 values were 20.6 °and -21.9°, consistent with a FIB-milling angle of 20° and opposite
253 orientation of the grids relative to the milling direction. The pre-tilt axis angles were
254 estimated as 171.8° and 183.8°, which is consistent with the error expected from manually
255 aligning the milling direction when inserting grids into the microscope.

256 To estimate the accuracy of the tilt estimation in tilt series, we calculated the mean absolute
257 difference between the tilt and axis-angle estimates and the fitted model, excluding the axis-
258 angle estimates at tilt angles under 5°. For the first tilt series we obtained accuracy estimates
259 of 2.08° and 2.58° for tilt and axis-angles, respectively. In the second tilt series the accuracy

260 estimates were 3.95° and 9.47°. In both cases the accuracy was lower than for the tilted
261 aquaporin crystals, presumably due to the relatively short exposure of each micrograph in
262 the tilt series. However, the substantially higher mean differences in the second tilt series
263 suggest that the accuracy is highly dependent on the quality of the underlying data.

264 **Sample thickness estimation**

265 Even after correcting for sample tilt we found that for FIB-milled samples we often could
266 observe Thon-ring like modulation in the power spectrum at higher resolution than
267 suggested by the goodness of fit estimate (Fig. 3b, top plot). These modulations are out of
268 phase with the predicted modulations, as described by (McMullan *et al.*, 2015) and
269 (Tichelaar *et al.*, 2020). We therefore implemented an extension of the CTF model as
270 described by (McMullan *et al.*, 2015) (Fig. 3a). For some images we found that the thickness
271 could be well estimated by assuming that the goodness of fit resolution estimate obtained
272 using the old model implemented in CTFFIND4 corresponds to the first node in the
273 modulation function, according to Eq. (7). With our new model, estimated CTF parameters
274 were very similar to those from CTFFIND4, but the fit in CTFFIND5 extended to higher
275 resolution (Fig. 3b).

276 In other images, mostly with defocus values under 1 μm and with a sample thickness over
277 200 nm, CTFFIND4 could fit the power spectrum before and after the first node using the
278 old CTF model, with some deviations between the fit and the power spectrum (Fig. 3c).
279 Fitting the power spectrum with the new model in CTFFIND5 resulted in substantially
280 different estimated CTF parameters and an improved fit, even though the goodness-of-fit
281 estimation did not change. Based on these results we conclude that CTFFIND5 will provide
282 more accurate CTF parameters for images of thick samples, such as those generated from
283 FIB-milling. In addition, the fit provides a direct readout of the specimen thickness, which is
284 important for judging specimen quality and the potential for high-resolution information
285 that can be recovered from these images.

286 **Estimating the accuracy of sample thickness estimation using the Lambert-Beer law on energy**
287 **filtered data**

288 CryoEM is frequently performed using an energy filter to remove inelastically scattered
289 electrons. The fraction of inelastically scattered electrons can be described by the Lambert-
290 Beer law, which states that the fraction of electrons removed from the image is
291 proportional to the thickness of the sample. The apparent mean free path for electron
292 scattering has been experimentally determined for common cryoEM conditions (Rice *et al.*,
293 2018). To test whether thickness estimation in CTFFIND5 is consistent with this method
294 we used a dataset of 655 exposures of a lamella of ER-HoxB8 cells collected using the DeCo-
295 LACE approach (Elferich *et al.*, 2022). We used CTFFIND5 to estimate the thickness t of
296 every exposure and plotted $-ln\left(\frac{I}{I_0}\right)$ against t (Fig. 4). Fitting the data to a linear model
297 described in Methods (Eq. (8)), we found that 568 out of 655 exposures followed closely a
298 linear relationship with a mean free path κ of 317 nm. Manual inspection of images that did
299 not follow this linear relationship revealed that they either contained visible ice
300 contamination, platinum deposits, or they were collected over ice without cellular features
301 and displayed weak Thon rings. The value of κ is consistent the value found by (Rice *et al.*,
302 2018), even though our dataset was collected without an objective aperture. The x-axis
303 intercept of the linear model was -14.1 nm, meaning that the node position systematically
304 predicts a smaller thickness than predicted by the Lambert-Beer law. This discrepancy is
305 further discussed in the next section. To estimate the accuracy of the sample thickness
306 determined by CTFFIND5 we calculated the mean absolute difference to the linear model,
307 which was 4.8 nm. These data suggest that sample thickness determination using node-
308 fitting is an alternative to using Lambert-Beers law that has the advantage of not relying on
309 the constant κ and the intensity I_0, both of which might not be readily available. Also, the
310 two approaches are complementary as they rely on orthogonal mechanisms.

311 **Estimating the accuracy of sample thickness estimation using tomography**

312 We used a dataset of seven micrographs collected from lamellae of ER-HoxB8 cells together
313 with tilt series collected afterwards from the same locations to verify the accuracy of the

314 thickness estimates obtained using CTFFIND5. We used CTFFIND5 to estimate the
315 thickness ($t_{CTFFIND}$) for every location and compared it with the thickness estimated from
316 the tomogram reconstructed from the tilt series (t_{TOMO}). We measured t_{TOMO} by manually
317 estimating the distance between the surfaces of the lamella in three different positions.
318 When we plotted $t_{CTFFIND}$ against t_{TOMO} we found that the values were highly correlated,
319 but t_{TOMO} was consistently smaller than $t_{CTFFIND}$ (Fig. 5). A linear fit revealed a slope of
320 0.95 and a y-axis intercept of 0.12 nm. This means that the CTFFIND5 thickness estimate is
321 on average 1.05x higher than the thickness estimated by tomography. (Tichelaar *et al.*,
322 2020) also report that estimating the thickness from the CTF nodes resulted in values
323 roughly 1.1x higher than estimated by tomography. The reasons for the systematic
324 discrepancies between thicknesses estimated by CTFFIND5 and estimates based on
325 Lambert-Beer's law and tomography are unclear, but since they are small and CTFFIND5
326 estimates lie in between the other two estimates, they will provide comparable
327 information.

328 **CTF estimation and correction assists biological interpretation of intermediate-magnification**
329 **lamella images**

330 During data collection of cryoEM data in cells, the operator frequently relies on images
331 taken at low magnification to select areas of interest and establish their biological context.
332 The pixel size of these images is usually about 40 Å, with a defocus of about 200 µm. This
333 produces strong contrast from biological membranes, but can sometimes also lead to
334 substantial fringes near these membranes (Fig. 6a). We found that a simple CTF correction
335 based on CTFFIND defocus estimates obtained from the overview images can reduce these
336 fringes (Fig. 6b). A simple CTF correction can be done using the program apply_ctf,
337 included with *cis*TEM, by phase flipping according to the fitted CTF (Fig. 6c). However, we
338 found that including a Wiener filter-based amplitude correction describe by (Tegunov &
339 Cramer, 2019) produces a more naturally looking image that might be best suited to
340 recognize cellular features (Fig. 6d).

341 **CTFFIND5 runtimes**

342 To gauge the ability of CTFFIND5 to provide real time feedback during cryoEM data
343 collection we measured its runtime on three representative micrographs (Table 2).
344 Without estimation of tilt or sample thickness CTFIND5 performed CTF estimation roughly
345 within a second. Estimation of the sample thickness adds roughly half a second to the
346 runtime, therefore allowing CTF estimation within a timeframe comparable to typical
347 exposure times. Estimation of the tilt on the other hand increased runtimes substantially to
348 the order of several minutes, due to the exhaustive search of potential tilts over hundreds
349 of powerspectra. While these runtimes are substantially slower than cryoEM data
350 acquisition, near real time estimation can be achieved by using multiple CPU cores.
351 Furthermore, optimization of the number of tiles used, better search algorithms, or
352 implementations employing GPUs could increase the speed to the point where real time
353 estimation is more feasible.

354 Conclusion

355 The new features implemented in CTFFIND5 improve CTF estimation from the power
356 spectra of cryoEM micrographs where assumptions made in its predecessor, CTFFIND4,
357 namely a thin and untilted sample, do not hold. The tilt of the sample is estimated by fitting
358 the CTF to the power spectra calculated from small patches across the image, similar to
359 other software including CTFTilt (Mindell & Grigorieff, 2003), Ctfplotter (Xiong *et al.*, 2009;
360 Mastronarde, 2024), goCTF (Su, 2019), and Warp (Tegunov & Cramer, 2019). After
361 estimation of the sample tilt a tilt-corrected power spectrum is produced that exhibits
362 stronger Thon rings at higher resolution.

363 To take into account the modulation of the power spectra by thick samples (Tichelaar *et al.*,
364 2020; McMullan *et al.*, 2015) we fit a modified CTF model, which increases the resolution of
365 the fitted regions of the spectra and provides a read-out of the sample thickness. While the
366 low exposures (3-5 e^-/A2) typically used in electron cryo-tomography often preclude
367 fitting of sample thickness from power spectra of individual images in the tilt series, we
368 demonstrate that this works reliably for higher exposures (~ 30 e^-/A2) typically used for

369 2D template matching (Lucas *et al.*; Rickgauer *et al.*, 2017) and in-situ single particle
370 analysis (Cheng *et al.*, 2023).

371 While these improvements are especially relevant for in-situ samples, e.g., prepared by
372 cryo-FIB milling, the analysis of images of purified samples recorded at lower acceleration
373 voltages, e.g., 100 keV (McMullan *et al.*, 2023), may also benefit since thickness-dependent
374 CTF modulations will appear at lower resolution with longer electron wavelengths (see Eq.
375 (6)). Per-micrograph CTF estimation can be followed by per-particle CTF refinement, as
376 implemented in *cis*TEM (Grant *et al.*, 2018), Relion (Kimanius *et al.*, 2021), or cryoSPARC
377 (Punjani *et al.*, 2017). The improvements of CTFFIND5 will provide better starting values
378 for this refinement, yielding better overall CTF estimation and recovery of high-resolution
379 information during 3D reconstruction.

380 In summary, the improvements implemented in CTFFIND5 result in more accurate CTF
381 estimation of thick and tilted samples and provide valuable information about the samples
382 to the microscopist.

383 Data availability

384 The images of tilted aquaporin crystals were previously published (Murata *et al.*, 2000) and
385 are available at https://grigoriefflab.umassmed.edu/tilted_aquaporin_crystals . The
386 untilted exposures of ER-HOXB8 cells are available at EMPIAR (EMPIAR-11063). The
387 tomograms and tilt series from ER-HOXB8 cells have been deposited to EMDB (EMD-
388 43419, EMD-43420, EMD-43424, EMD-43425, EMD-43427, EMD-43428, EMD-43429) and
389 EMPIAR (EMPIAR-11854), respectively. The source code for CTFFIND5 is available at
390 https://github.com/GrigorieffLab/cisTEM/tree/ctffind5 and binaries for most Linux
391 distributions can be downloaded at https://cistem.org/development .

392 Acknowledgments

393 We would like to thank members of the Grigorieff lab for testing CTFFIND5 and helpful
394 discussion. We furthermore thank Benjamin Himes for helpful discussions and code review
395 within *cis*TEM. We thank Alexis Rohou for comments on the manuscript. L.K. and N.G.

gratefully acknowledge funding from the Chan Zuckerberg Initiative, grant #2021-234617 (5022).

Author contributions

Conceptualization: J.E. and N.G.; Data curation: J.E., L.K. and X.Z.; Formal analysis: J.E., L.K., X.Z. and N.G.; Funding acquisition: N.G.; Investigation: J.E., L.K. and X.Z.; Methodology: J.E., L.K. and N.G.; Project administration: J.E. and N.G.; Resources: J.E. and N.G.; Software: J.E., L.K. and N.G.; Supervision: J.E. and N.G.; Validation: J.E., L.K., X.Z. and N.G.; Visualization: J.E., L.K. and X.Z.; Writing – original draft: J.E., L.K., X.Z. and N.G.; Writing - review & editing: J.E., L.K., X.Z. and N.G.;

Tables

Table 1: Comparison of CTFFIND5 estimation of sample tilt with crystallographic analysis

Image	Axis angle φ			Tilt angle θ		
	crystallog.	ctffind5	$\Delta\varphi$	crystallog.	ctffind5	$\Delta\theta$
530394	93.28	94.98	-1.7	19.6	20.69	-1.09
530419	109.78	106.51	3.27	18.66	16.04	2.62
530430	104.38	101.13	3.25	21.32	20.37	0.95
530444	98.39	97.62	0.77	20.72	20.88	-0.16
660027	99.68	102.34	-2.66	19.4	22.39	-2.99
540149	94.45	85.84	8.61	43.08	44.59	-1.51
540291	96.16	98.1	-1.94	45.11	40.68	4.43
540302	93.98	93.39	0.59	44.7	44.21	0.49
540313	95.34	95.13	0.21	44.03	46.49	-2.46
660183	97.69	97.27	0.42	48.13	48.99	-0.86
550069	90.08	92.55	-2.47	60.46	60.83	-0.37
550089	91.48	92.04	-0.56	60.5	60.72	-0.22
660291	93.23	92.19	1.04	57.59	59.19	-1.60
660421	89.32	89.06	0.26	61.36	60.01	1.35

680341	89.67	90.02	-0.35	58.68	59.62	-0.94
530345	N/A	108.6		0	0.84	-0.84
530356	N/A	231.17		0	1.93	-1.93
530358	N/A	56.58		0	1.29	-1.29
530375	N/A	3.21		0	0.79	-0.79
530378	N/A	67.6		0	2.17	-2.17

409 **Table 2:** Runtime of CTFFIND5 on representative micrographs

Micrograph		1	2	3
Image properties				
Image size		4070x2892	2880x2046	4746x3370
Pixel size (Å)		1.5	4.175	2.5
Runtime (s)				
Tilt	Thickness			
-	-	0.9±0.1	0.7±0.1	1.7±0.1
+	-	39.0±0.2	208±1	173.4±0.1
-	+	1.4±0.1	1.3±0.1	2.4±0.1
+	+	39.5±0.1	209±1	173.0±0.1

410

Figures

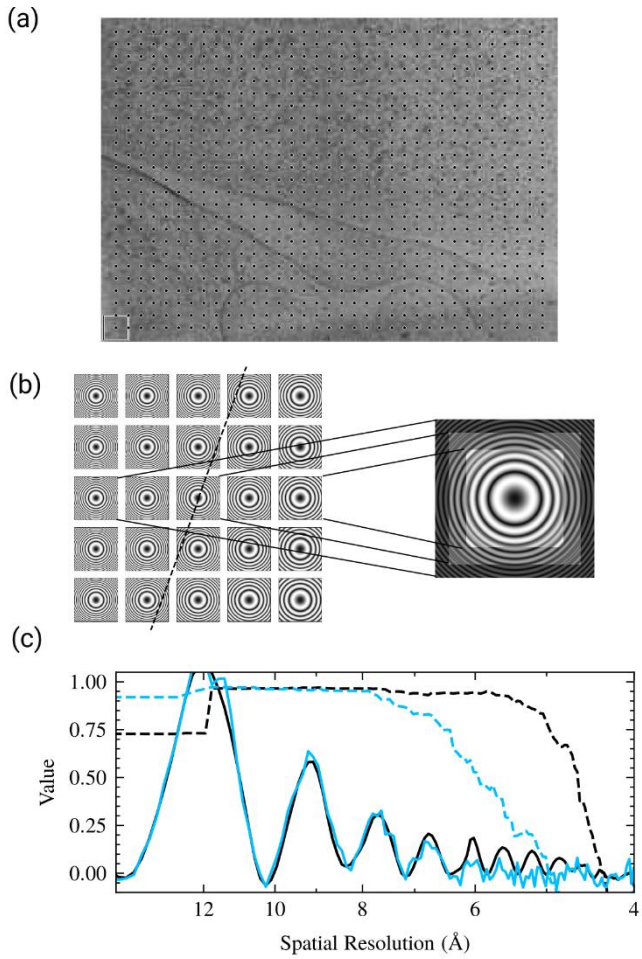

Figure 1: Tilt estimation and correction in CTFFIND5. (a) Power spectra are calculated in 128x128 pixel patches as indicated on a representative micrograph. The dots represent the locations of the patches and the boxes indicate patch size. (b) A model of the expected power spectrum in each patch given an average defocus Δf, tilt angle θ, and tilt axis ϕ is compared to the actual power spectra of tiles. After an optimal set of θ and ϕ has been found a corrected power spectrum is calculated by summing the tile power spectra, scaled to correct for the defocus difference. (c) Comparison of the original power spectrum (solid line, blue) to the tilt-corrected power spectrum (solid line, black). The tilt-corrected power spectrum exhibits clear peaks at higher spatial resolution than the uncorrected power spectrum, as evident by the "goodness-of-fit" scores (dashed lines). The estimated CTF

parameters are $\Delta f_1 = 10603$ Å, $\Delta f_2 = 10193$ Å, $\alpha = 85.9°$ for the uncorrected power spectrum and $\Delta f_1 = 10492$ Å, $\Delta f_2 = 10342$ Å, $\alpha = 81.2°$, $\theta = 12.3°$, $\phi = 261.6°$ for the tilt-corrected power spectrum. The fit resolution is 5.9 Å for the uncorrected power spectrum (dashed line, blue) and 4.6 Å for the tilt-corrected spectrum (dashed line, black).

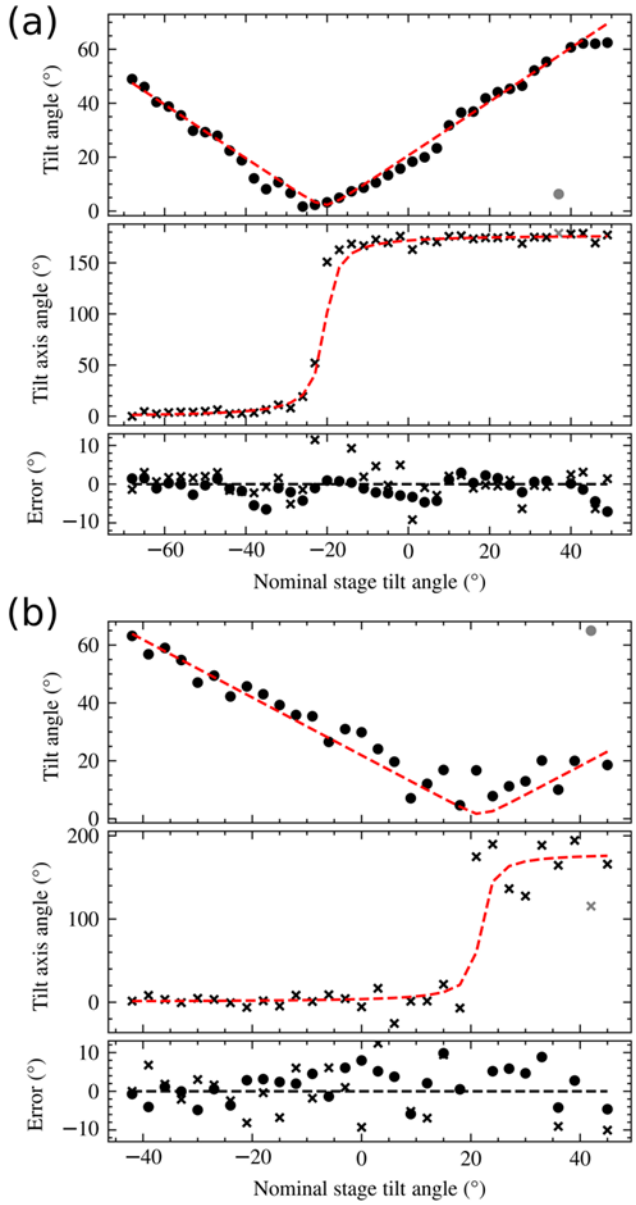

Figure 2: Validation of tilt estimation using tilt series data. (a) Estimated tilt angle and axis of 40 micrographs of a tilt series taken on a FIB-milled biological specimen. For each image the tilt angle (dots, upper plot) and tilt axis direction (crosses, middle plot) are plotted as a function of the nominal stage angle. The data were fitted to a model of the specimen tilt and constant stage tilt axis before tilting the stage. The estimated stage tilt axis has an angle of 171.8° and the estimated specimen pre-tilt is 20.6° with a tilt axis of 171.8°, which is consistent with the FIB-milling angle of 20° and manual alignment of the milling direction to the goniometer tilt axis. In the bottom plot the fit residuals for tilt angle and axis are

plotted. (b) Data for another tilt series plotted as described for (a). The estimated stage tilt axis is 179.8°, the estimated specimen pre-tilt is -21.9° with a tilt axis of 183.8°. This is consistent with this grid being inserted in the opposite orientation as the grid shown in (a), but still with a rough alignment of milling direction and tilt axis.

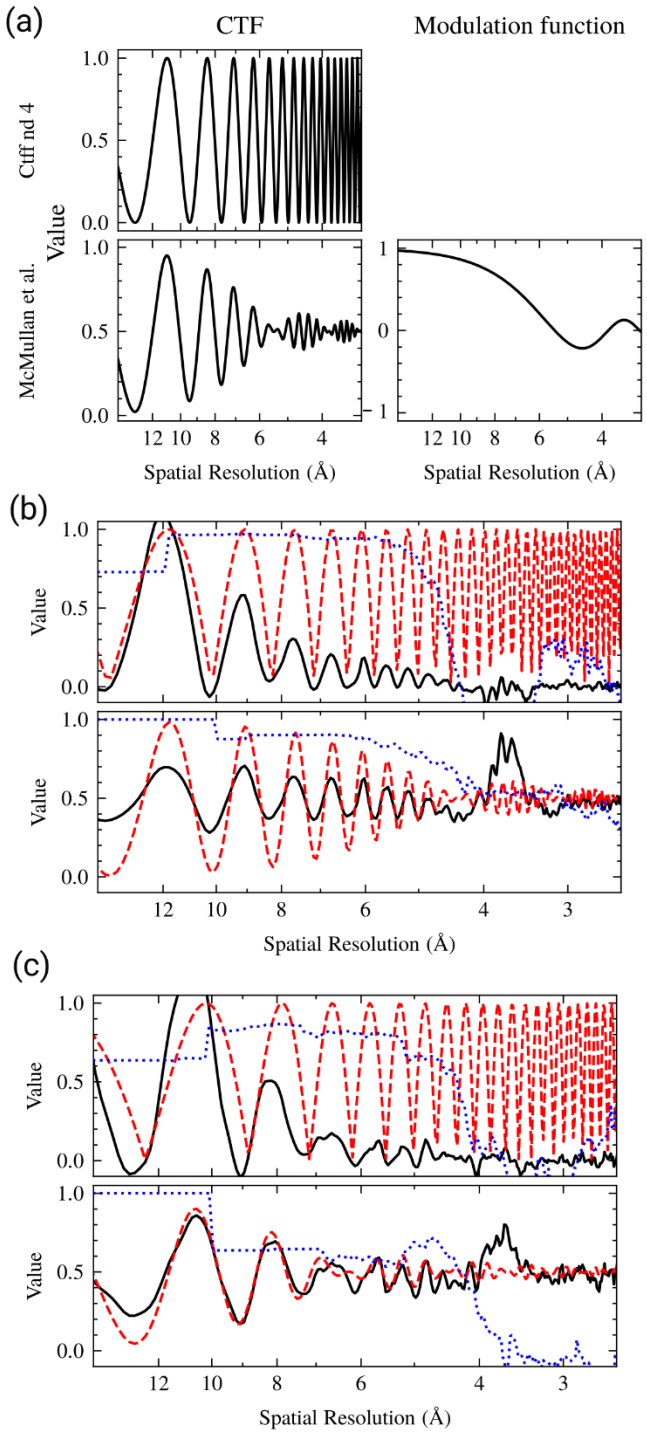

Figure 3: Sample thickness estimation by fitting Thon ring patterns. (a) Comparison of the CTF model used in CTFFIND4, and after applying the modulation function (right) described by (McMullan *et al*., 2015). (b) Representative example of Thon ring fitting in a lamella without (top) and with (bottom) thickness estimation. The tilt of the specimen was

estimated to be 12.3°. When fitting without thickness estimation the estimated parameters were $\Delta f_1 = 10492$ Å, $\Delta f_2 = 10342$ Å, $\alpha = 81.2°$. When taking sample thickness into account the estimated parameters were $\Delta f_1 = 10481$ Å, $\Delta f_2 = 10286$ Å, $\alpha = 69.6°$, $t = 969$ Å. The estimated fit resolution was 4.6 Å and 3.4 Å without and with sample estimation, respectively. (c) Representative example of Thon ring fitting in a lamella without (top) and with (bottom) thickness estimation. The tilt of the specimen was estimated to be 6.7°. When fitting without thickness estimation the estimated parameters were $\Delta f_1 = 8002$ Å, $\Delta f_2 = 7717$ Å, $\alpha = 73.4°$. When taking sample thickness into account the estimated parameters were $\Delta f_1 = 8549$ Å, $\Delta f_2 = 8343$ Å, $\alpha = 63.3°$, $t = 2017$ Å. The estimated fit resolution was 4.3 Å and 4.2 Å without and with sample estimation, respectively.

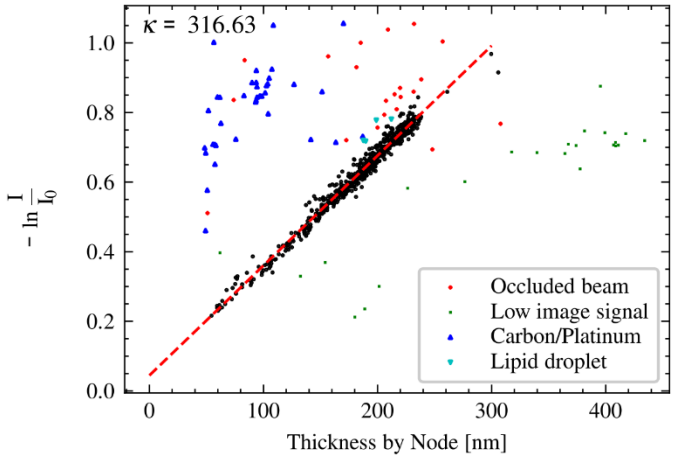

Figure 4: Validation of sample thickness estimation in CTFFIND5 by comparing the estimates to the intensity attenuation by the zero-loss energy filter. An estimation of the linear relationship using the RANSAC algorithm results in a slope of 1/316.6 nm and an x-axis intercept at -14 nm (red dashed line). Data points that were labeled as outliers by the RANSAC algorithm were manually inspected and color-coded according to visual inspection of the micrographs.

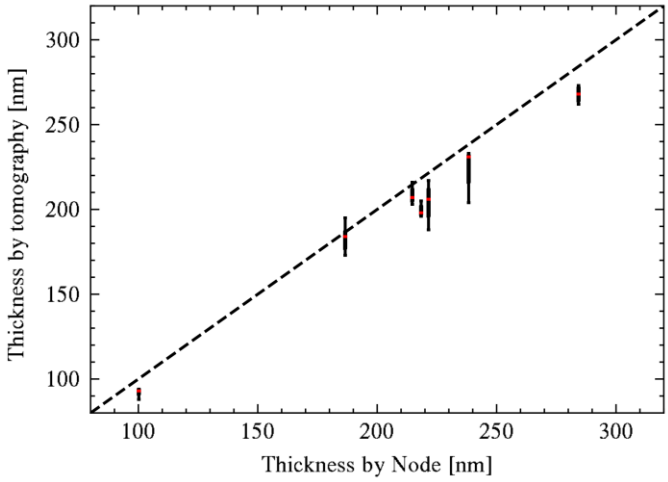

Figure 5: Validation of sample thickness estimation in CTFFIND5 by tomography. The distribution of thickness measurements in seven tomograms are shown as box plots with the median indicated by a red line. The position on the x-axis corresponds to the thickness estimate by CTFFIND5. The black dashed line indicates identity.

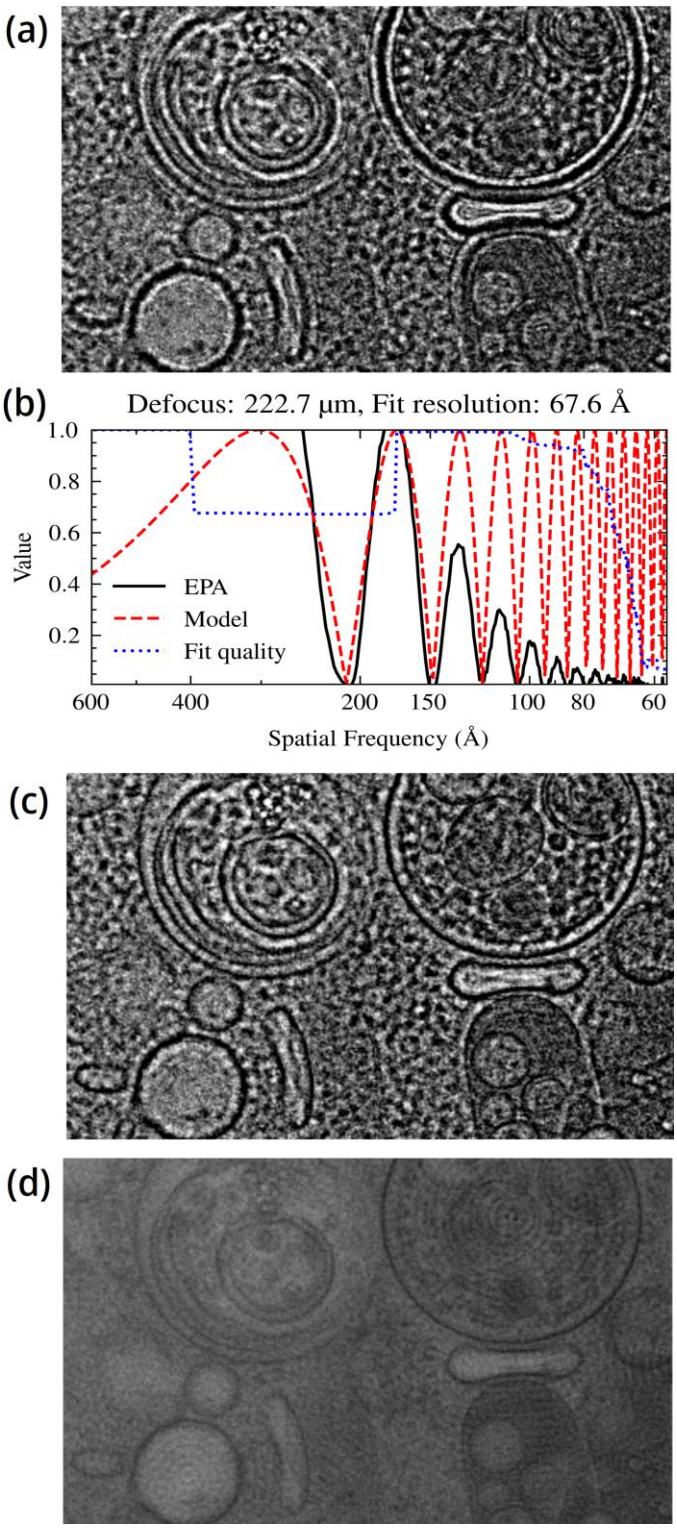

Figure 6: CTF correction of medium magnification overviews. (a) Representative area of a micrograph of a cellular sample at a pixel size of 40 Å without CTF correction. (b) Fit of the

power spectrum of the micrograph shown in panel a CTF model. (c-d) The same micrograph as shown in panel (a) after CTF correction by phase flipping (c) or with a Wiener-like filter (d)

Bibliography

Cheng, J., Liu, T., You, X., Zhang, F., Sui, S.-F., Wan, X. & Zhang, X. (2023). *Nat Commun* **14**, 1282.

Elferich, J., Schiroli, G., Scadden, D. T. & Grigorieff, N. (2022). *Elife* **11**, e80980.

Grant, T., Rohou, A. & Grigorieff, N. (2018). *Elife* **7**, e35383.

Hagen, W. J. H., Wan, W. & Briggs, J. A. G. (2017). *Journal of Structural Biology* **197**, 191–198.

Kimanius, D., Dong, L., Sharov, G., Nakane, T. & Scheres, S. H. W. (2021). *Biochemical Journal* **478**, 4169–4185.

Lucas, B. A., Himes, B. A., Xue, L., Grant, T., Mahamid, J. & Grigorieff, N. *eLife* **10**, e68946.

Mastronarde, D. N. (1997). *Journal of Structural Biology* **120**, 343–352.

Mastronarde, D. N. (2005). *J Struct Biol* **152**, 36–51.

Mastronarde, D. N. (2024). *J Struct Biol* **216**, 108057.

Mastronarde, D. N. & Held, S. R. (2017). *J Struct Biol* **197**, 102–113.

McMullan, G., Naydenova, K., Mihaylov, D., Yamashita, K., Peet, M. J., Wilson, H., Dickerson, J. L., Chen, S., Cannone, G., Lee, Y., Hutchings, K. A., Gittins, O., Sobhy, M. A., Wells, T., El-Gomati, M. M., Dalby, J., Meffert, M., Schulze-Briese, C., Henderson, R. & Russo, C. J. (2023). *Proceedings of the National Academy of Sciences* **120**, e2312905120.

McMullan, G., Vinothkumar, K. R. & Henderson, R. (2015). *Ultramicroscopy* **158**, 26–32.

Mindell, J. A. & Grigorieff, N. (2003). *J Struct Biol* **142**, 334–347.

Murata, K., Mitsuoka, K., Hirai, T., Walz, T., Agre, P., Heymann, J. B., Engel, A. & Fujiyoshi, Y. (2000). *Nature* **407**, 599–605.

Pedregosa, F., Varoquaux, G., Gramfort, A., Michel, V., Thirion, B., Grisel, O., Blondel, M., Prettenhofer, P., Weiss, R., Dubourg, V., Vanderplas, J., Passos, A., Cournapeau, D., Brucher, M., Perrot, M. & Duchesnay, E. (2011). *Journal of Machine Learning Research* **12**, 2825–2830.

Punjani, A., Rubinstein, J. L., Fleet, D. J. & Brubaker, M. A. (2017). *Nat Methods* **14**, 290–296.

Rice, W. J., Cheng, A., Noble, A. J., Eng, E. T., Kim, L. Y., Carragher, B. & Potter, C. S. (2018). *J Struct Biol* **204**, 38–44.

Rickgauer, J. P., Grigorieff, N. & Denk, W. (2017). *eLife* **6**, e25648.

Rohou, A. & Grigorieff, N. (2015). *J Struct Biol* **192**, 216–221.

Su, M. (2019). *Journal of Structural Biology* **205**, 22–29.

Tegunov, D. & Cramer, P. (2019). *Nat Methods* **16**, 1146–1152.

Thon, F. (1971). Vol. *Electron Microscopy in Material Science*. pp. 570–625. Academic Press New York.

Tichelaar, W., Hagen, W. J. H., Gorelik, T. E., Xue, L. & Mahamid, J. (2020). *Ultramicroscopy* **216**, 113023.

Xiong, Q., Morphew, M. K., Schwartz, C. L., Hoenger, A. H. & Mastronarde, D. N. (2009). *Journal of Structural Biology* **168**, 378–387.